Journal of Colloid and Interface Science 446 (2015) 67–76

Contents lists available at ScienceDirect

Journal of Colloid and Interface Science

www.elsevier.com/locate/jcis

Simulation of chaotic electrokinetic transport: Performance of commercial software versus custom-built direct numerical simulation codes

Elif Karatay, Clara L. Druzgalski, Ali Mani *

Department of Mechanical Engineering, Stanford University, Stanford, CA 94305, USA
Center for Turbulence Research, Stanford University, Stanford, CA 94305, USA

GRAPHICAL ABSTRACT

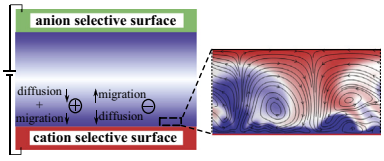

ARTICLE INFO

Article history:
Received 27 October 2014
Accepted 23 December 2014
Available online 14 January 2015

Keywords:
Concentration-polarization
Overlimiting current
Electroosmotic instability
Comsol
Direct numerical simulation

ABSTRACT

Many microfluidic and electrochemical applications involve chaotic transport phenomena that arise due to instabilities stemming from coupling of hydrodynamics with ion transport and electrostatic forces. Recent investigations have revealed the contribution of a wide range of spatio-temporal scales in such electro-chaotic systems similar to those observed in turbulent flows. Given that these scales can span several orders of magnitude, significant numerical resolution is needed for accurate prediction of these phenomena. The objective of this work is to assess accuracy and efficiency of commercial software for prediction of such phenomena. We have considered the electroconvective flow induced by concentration polarization near an ion selective surface as a model problem representing chaotic elecrokinetic phenomena. We present detailed comparison of the performance of a general-purpose commercial computational fluid dynamics (CFD) and transport solver against a custom-built direct numerical simulation code that has been tailored to the specific physics of unsteady electrokinetic flows. We present detailed statistics including velocity and ion concentration spectra over a wide range of frequencies as well as time-averaged statistics and computational time required for each simulation. Our results indicate that while accuracy can be guaranteed with proper mesh resolution and avoiding numerical dissipation, commercial solvers are generally at least an order of magnitude slower than custom-built direct numerical simulation codes.

© 2015 Elsevier Inc. All rights reserved.

1. Introduction

Recent investigations have revealed that electrokinetic phenomena can induce chaotic flows in a wide range of conditions, including those involving ion-selective interfaces [1–4] and interfaces with conductivity gradients [5–8]. In such systems the nonlinearities responsible for chaos arise from electrostatic forces and not fluid inertia. Therefore hydrodynamic instabilities in these systems are not bound by the Reynolds number and can exist even in micron-scale spaces with practically zero Reynolds number [9]. In other words, the chaotic transport phenomena arising from such instabilities has relevance to a wide range of micro- and macroscale systems with applications spanning from conventional electrodialysis for water purification/desalination, edible salt

* Corresponding author at: Department of Mechanical Engineering, Stanford University, Stanford, CA 94305, USA.
E-mail address: alimani@stanford.edu (A. Mani).

http://dx.doi.org/10.1016/j.jcis.2014.12.081
0021-9797/© 2015 Elsevier Inc. All rights reserved.

production, recovery of acids in metal finishing industries [2,10,11], traditional electrochemical processes such as electrodeposition [12] or electrochemical machining [13] to micro/nanofluidic separations [14,15], sample preconcentration and detection [16].

A common scenario that can trigger chaotic electrokinetic flow, is when ions are selectively driven from a fluid electrolyte to an ion-selective medium, such as a membrane, electrode, or array of nanochannels. A demonstration of this configuration is shown in Fig. 1a. Once an electric field is applied normal to a charge-selective surface, for sufficiently low voltages ion transport reveals an ohmic behavior. At higher voltages, up to an order of 10 thermal voltage, ion concentration gradients near the ion-selective surface become sharper, leading to the well known diffusion-limited transport phenomena associated with ion concentration polarization (CP) [1,2]. In this regime, classical theory predicts an electroneutral solution in the bulk and a thin electric double layer (EDL) next to the interface [17,18]. For even higher voltages, overlimiting conductance (OLC), beyond the diffusion limitation, has been demonstrated in numerous experiments [19–22]. Moreover in the OLC regime, electrokinetic flows have been shown to arise in electrolyte solutions adjacent to charge-selective or polarizable interfaces in experimental [19,20,23–25], theoretical [26–30] and numerical studies [20,31,32]. The non-equilibrium EDLs, formed due to severe CP conditions, are shown to be hydrodynamically unstable [26,27]. This instability, referred to as electroosmotic instability (EOI) (also as electroconvective instability), can trigger chaotic vortices [9]. One of the key mechanisms of conductance beyond the diffusion limit is advective transport by these vortices [2].

Until very recently, theoretical and numerical investigations of OLC employed either one-dimensional models [31] or methods of matched asymptotics [28] which under-predict the experimentally measured ion-fluxes due to missing hydrodynamic effects. Initial calculations capturing EOI, used solutions to the electroneutral equations and lumped all electrostatic effects into an effective slip boundary condition derived using quasi-steady assumption [20,32]. These simulations were limited in accuracy since they predicted only steady response in the form of arrays of counter rotating vortex pairs. Recently there have been few two-dimensional direct numerical simulations (DNSs) [9,33–35] as well as three-dimensional DNSs [36,37] of EOI solving for the fully coupled Poisson–Nernst–Planck and Navier–Stokes equations. The DNSs reported in Refs. [9,34] revealed electrokinetic instability and transition to chaotic flows beyond a threshold value of applied electric potential, $\sim \mathcal{O}(1)$ V. Transitions from regular coherent vortex pairs to chaotic multi-scale vortex structures have been reported around the same voltage range. As shown in detail in Ref. [9], in the highly chaotic regime, the conventionally described quasi-steady charge layer is completely disrupted as the multi-scale vortices eject patches of positive and negative charge towards the bulk of the electrolyte solution. Some numerical investigations have also suggested the presence of different unsteady chaotic modes [33] and hint different kinds of bifurcations at various system-dependent critical voltages [34,35].

Capturing the dynamic nature of such systems in a simulation requires crafting a careful numerical methodology that can resolve various phenomena over a wide range of spatiotemporal scales: from nanometer scale electric double layers to micron (even sub-millimeter) scale vortices, and from charge relaxation time on the order of nanoseconds to chaos development time on the order of seconds. To overcome this challenge, very recent reports on DNS of electrokinetic chaos have employed custom-made codes tailored to the specific physics [9,33,34]. However, there has been no investigation on the efficiency and accuracy of general-purpose commercial computational fluid dynamics (CFD) software for the prediction of chaotic electrokinetic phenomena.

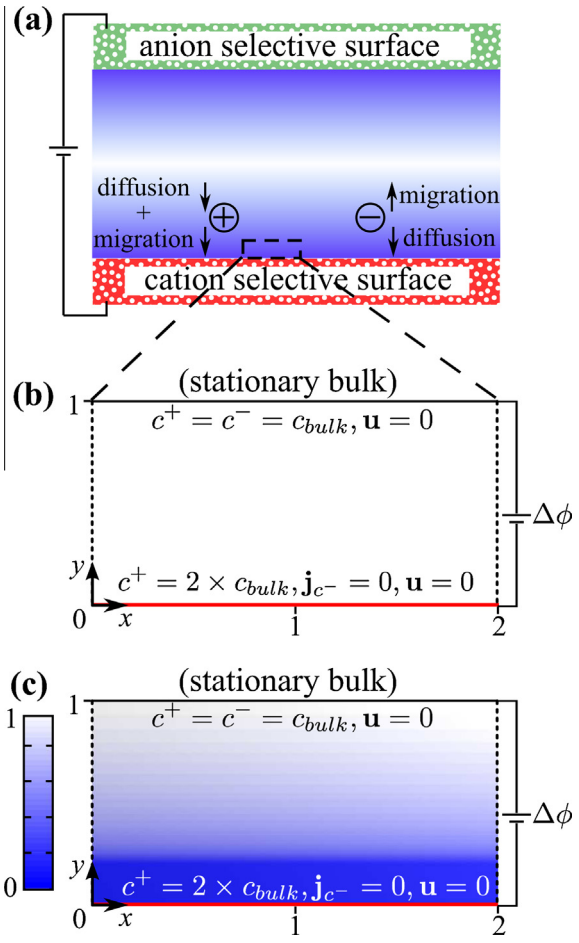

Fig. 1. Model problem and computational domain. (a) Schematic plot of salt concentration distribution in between anion and cation selective surfaces. (b) Computational domain with an aspect ratio of 2. (c) Stationary anion concentration c^- profile obtained from steady calculations. Color bar shows dimensionless c^- variation. (For interpretation of the references to color in this figure legend, the reader is referred to the web version of this article.)

General-purpose commercial CFD software can be attractive due to their easy-to-use-environment providing integrated packages for mesh generation in complex geometries, various built-in solvers applicable to a broad range of physical systems governed by PDEs and post-processing visualization tools. However, to ensure numerical robustness, these software often employ numerical algorithms that tend to smooth fields in the space–time domain. Examples of such methods include, spatial discretization of fluxes via upwind, or total variation diminishing (TVD) methods and time integration via global implicit solvers. These methods are appropriate for systems that are inherently smooth, such as laminar flows and heat transfer problems. These methods are also appropriate for turbulence closure models, since they aim to capture only the smooth time-averaged fields and not the volatile instantaneous picture.

Chaotic systems however, by nature compete against smoothness, and the question remains whether numerical smoothing can impose a conflicting constraint when commercial software are used for simulation of such systems. The answer to this question depends on the specific physical problem and there have been several attempts in literature to study the performance of commercial CFD codes in both laminar and turbulent flows for various applications [38–41]. Previous reports indicate that detailed comparative analyses are crucial when simulating complex flows, where a wide-range of spatio-temporal scales are involved

[38,42]. In the context of turbulent flows, flow over a cylinder is one of the extensively studied yet challenging turbulent flows exhibiting various regimes with different modes of instabilities [42–46]. The comparisons of the detailed turbulent statistics have indicated the notorious impact of numerical dissipation on the high wave number fluctuations [42].

We should note that any numerical method with finite order of accuracy would eventually provide accurate solutions in the limit of very high resolution, including those involving artificial smoothing. Therefore, in this context the relevant question is for a fixed resolution specified by the physical length scale of a system, how different numerical methods compare. In standard turbulence, the Kolmogorov length, η, is the length scale of the smallest eddies which must be resolved for a correct DNS. Given that η is typically orders of magnitude smaller than macroscale length l, even resolving η imposes significant computational cost and a good numerical method should not require a resolution smaller than that. Numerical analysis reveals that use of dissipative discretization on a mesh with resolution of order η effectively introduces an artificial diffusivity of order ηu, where u is the characteristic velocity of the flow. From turbulence theory the physical diffusion for such a system is on the order of $\eta u \times (\eta/l)^{1/3}$ [47]. In other words, under standard resolution, artificial diffusion induced by numerical dissipation can be larger than physical diffusion by a factor of $(l/\eta)^{1/3}$. This factor can be even higher than an order of magnitude for a highly turbulent flow. Chaotic electrokinetic flows are shown to exhibit fields and signals very similar to turbulent flows, including multi-layer vortex structures, and broadband energy spectra. This qualitative similarity and the physical tendency of the system to break smoothness, impel the necessity of evaluating the performance of commercial solvers for chaotic electrokinetic flows [9].

In this paper, we consider transient direct numerical simulations of the coupled Poisson–Nernst–Planck (PNP) and Navier–Stokes (NS) equations in 2D for a highly chaotic flow regime. We present comparison of the performance of a general-purpose CFD package against a verified custom-built DNS code (referred to as reference DNS herein) that is optimized specifically for chaotic electrokinetic phenomena. Among various commercial solver alternatives, we have chosen Comsol Multiphysics being frequently employed in the relevant research fields such as membrane science [48,49], microfluidics [50,7,51–53] and electrochemistry [54,55] where the effects of non-equilibrium EDL physics can be crucial. Moreover Comsol Multiphysics have been used in recent reports on nonlinear effects in electrokinetics [56–59].

Here, we study the efficiency of commercial software for the prediction of chaotic electrokinetic phenomena for the first time. As a measure of efficiency, we report the compute time against the reference code for a wide range of resolutions. To assess the impact of implicit solvers, we present comparison of detailed statistical analysis of mean transport and fluctuations, including energy spectra of concentration and velocity fields. In addition, we perform calculations by intentionally selecting dissipative solver options to assess the impact of numerical dissipation on the predicted statistics in chaotic electrokinetic regimes.

2. Model problem

Fig. 1a shows a system consisting of an electrolyte solution in between an anion selective surface and a cation selective surface, *e.g.* anion and cation exchange membranes in an electrodialysis system. Once an electric field is applied across this system, concentration gradients establish due to CP, leading to salt depletion near ion selective surfaces. Schematically depicted in Fig. 1a is the one-dimensional transport at low voltages while the bulk of the solution is still stationary. We here consider a representative (mathematical) model problem allowing us to capture electrokinetic chaos with less computational cost. Adopting after the same reduced models in the literature [1,2,24,29] we consider a subregion near only one membrane (Fig. 1b and c) and introduce artificial boundary conditions at some distance L from the membrane where the domain is truncated. We note that this model problem is not quantitatively representative of the full problem, but it allows us to focus on the essential physics of chaotic electrokinetic transport, and is certainly a relevant model for the purpose of assessing numerical methods. Our computational domain is periodic in the tangential direction x – with an aspect ratio of 2, as shown in Fig. 1b. For a fair comparison of the commercial and the reference DNS codes, we consider this system which can be simulated by a single core, excluding the potential effects of parallelization efficiency of the codes.

We solve for the electric potential distribution, ion and momentum transport for a dilute solution of a monovalent symmetric strong salt. Incompressible Navier–Stokes and Nernst–Planck–Poisson equations describe the flow, ion distribution and electric potential respectively.

$$\rho\frac{\partial \boldsymbol{u}}{\partial t} = -\boldsymbol{\nabla} p + \mu\boldsymbol{\nabla}^2\boldsymbol{u} + \rho_e\boldsymbol{E} \tag{1a}$$

$$\boldsymbol{\nabla}\cdot\boldsymbol{u} = 0 \tag{1b}$$

$$\frac{\partial c^{\pm}}{\partial t} = -\boldsymbol{\nabla}\cdot(c^{\pm}\boldsymbol{u} - D\boldsymbol{\nabla}c^{\pm} \mp DV_T^{-1}c^{\pm}\boldsymbol{\nabla}\phi) \tag{1c}$$

$$-\varepsilon\boldsymbol{\nabla}^2\phi = \rho_e \tag{1d}$$

where $\boldsymbol{u} = u\hat{x} + v\hat{y}$ is the velocity vector field. p, c^+, c^- and ϕ are hydrodynamic pressure, cation concentration, anion concentration and electric potential, respectively. Here $\boldsymbol{E} = -\boldsymbol{\nabla}\phi$ is the electric field. ρ_e is the free charge density given by $ze(c^+ - c^-)$ for a monovalent symmetric salt (here ionic valence $z = \pm 1$). ρ, μ, ε and D are the mass density, viscosity, dielectric permittivity of the fluid and diffusion coefficient of ions respectively. Moreover, $V_T = k_BT/ze$ is the thermal voltage where k_B and e are Boltzmann constant and elementary charge, respectively.

The Eqs. (1a)–(1d) are solved in 2D with the boundary conditions demonstrated in Fig. 1b and c. Here the spatial coordinates are scaled by the surface-to-bulk distance L. On the cation selective surface at $y = 0$, there is no-slip, $\boldsymbol{u} = 0$, and the potential is grounded, $\phi = 0$. We implement the ion selectivity at $y = 0$ by enforcing a no-flux condition for anions, $\boldsymbol{j}_{c^-} = 0$, and fixed cation concentration twice of the bulk concentration, $c^+ = 2 \times c_{bulk}$, adopting after previous models [29]. On the upper boundary at $y = 1$ which is representative of a stationary homogeneous bulk solution, there is no-slip, $\boldsymbol{u} = 0$, and the concentrations of both anions and cations are equal to the bulk salt concentration, $c^+ = c^- = c_{bulk}$. We implement the applied voltage $\phi = \Delta\phi$ at $y = 1$. We employ periodic boundary conditions for all variables between the boundaries $x = 0$ and $x = 2$.

In the Navier–Stokes equations (Eq. (1a)), we neglect the nonlinear terms $\rho\boldsymbol{u}\cdot\boldsymbol{\nabla}\boldsymbol{u}$. Our inspections verified that over the entire domain, this term is at least few orders of magnitude smaller than the other terms. Our previous analyses [9] performed for the same model problem revealed that the inertial terms are negligible compared to the viscous terms for dilute aqueous salt solutions at the explored range of voltages.

The key dimensionless parameters of our model problem are the (i) electrohydrodynamic coupling constant $\kappa = \varepsilon V_T^2/(\mu D)$ (ii) dimensionless Debye screening length $\epsilon = \lambda_D/L$ where $\lambda_D = \sqrt{\varepsilon k_BT/[2(ze)^2 c_{bulk}]}$ is the dimensional Debye length and L is the domain size in transverse direction $y-$, (iii) dimensionless applied potential $\Delta\phi/V_T$. The employed electrohydrodynamic

coupling constant κ is chosen to be 0.5 corresponding to typical dilute aqueous salt solutions. We consider a dimensionless Debye length ϵ of 10^{-3} representative of *e.g.* a salt solution with $c_{bulk} = 1$ mM in a $L = 10$ μm gap. In this paper aiming at a comparative study of electrokinetic chaos solved by a commercial software and a reference DNS, we perform simulations at a fixed dimensionless applied voltage of $120V_T$, *i.e.* 3 *V*, which is reported to be well-above the onset of the chaotic regime ($\geqslant 40V_T$) in Ref. [9].

3. Numerical methods

The governing equations are solved by (i) commercial CFD package Comsol Multiphysics v4.4 using finite element methods and (ii) a reference DNS code, custom-built for electrokinetic flows using finite difference schemes. To resolve the EDL, a non-uniform mesh is used in the *y*-direction normal to the interface whereas a uniform mesh is used in the tangential *x*-direction. To provide an initial condition for the system, we first solve the steady Nernst–Planck–Poisson Eqs. (1c) and (1d) without the flow. Shown in Fig. 1c is the resultant steady anion concentration field, corresponding to the traditional steady description. Then the initial condition for the transient calculations is generated by applying a locally 1% random perturbation to the anion and cation concentration fields obtained from the steady calculation. The dimensionless time step used for all calculations is 10^{-6} scaled by diffusion time $t_{diff} = L^2/D$. All the simulations are performed on Intel Xeon E5620 CPUs.

For a fair comparison between the two codes, an effort has been made to eliminate the uncertainties that can be associated with the computational grid, implementation of boundary conditions and solution methodology. For example, a cartesian grid with the same stretching function in the *y*-direction has been used in the simulations by both codes. We match the computational grids by means of either the number of mesh points or the number of degrees of freedom (DOF). However it is important to note that there are basic differences between the two codes; such as numerical schemes and time discretization. Below we describe the computational details for both Comsol and the reference DNS code.

3.1. Comsol set up

All the Eqs. (1a)–(1c) and (1d) are solved through a GUI-based mathematics module allowing for implementation of user-defined transport equations. The concentration fields (1c) are implemented in general PDE form. The potential distribution (1d) is implemented in the pre-defined Poisson's equation. All the scalar fields are solved using quadratic Lagrange interpolation functions for space discretization. Among options for treating the boundary fluxes, the option with no smoothing was selected. Navier–Stokes and continuity Eqs. (1a) and (1b) are implemented in weak formulation. Quadratic Lagrange shape functions are used for NS equations whereas linear order was used for the continuity equation.

For the transient calculations, a time-segregated solver is used where the flow and pressure are solved in the first segregated step followed by the second step for concentrations and potential at each time step. For both steps a multifrontal massively parallel sparse direct solver (MUMPS) is employed. Different time stepping methods are employed for comparison purposes. First, a time discrete solver is used with two time discrete levels employing second order implicit backward differentiation [60]. Second a generalized-α method is used. Generalized-α is an implicit, second-order method with a parameter α ($0 \leqslant \alpha \leqslant 1$) to control the damping of high frequencies, where numerical damping is higher for smaller α [60]. Several values of α ($= 0.1, 0.4, 0.8$ and 0.99) are employed to study the effect of numerical dissipation on the prediction of chaotic transport.

Although unstructured grids can be used in FEM based Comsol, the simulations were performed on the same structured grid as in the reference DNS code with different resolutions to confirm the mesh independency of the solution in the vicinity of the membrane boundary. The scaled *y*-direction length is 1 with N_y mesh points and the scaled *x*-direction width is 2 with N_x mesh points. We present results for two mesh resolutions. First the number of grid points and second the number of degrees of freedom, with the considerations of fourth order interpolation functions in the Comsol code, are matched with the mesh used in the reference DNS code. Table 1 summarizes the employed grid sizes for mesh refinement study.

3.2. Reference DNS set up

Our previous work [9] presents a comprehensive analysis of electroconvective chaos near ion-selective membranes by introducing a custom-made DNS code. We have adopted the same computational strategy here.

In the reference DNS code, the fluxes of mass and momentum are discretized using the second order central finite difference scheme on a structured mesh. To allow the use of the most compact stencil, we employ a staggered mesh configuration on which concentration, electrostatic potential, and pressure are solved on cell centers, and velocities, electric field, and ion fluxes are computed on the faces of each control volume. Given the statistical homogeneity of the problem in the tangential direction, we use a uniform mesh with periodic boundary conditions in this direction. In the interface-normal direction a nonuniform mesh is used. Near the interface the mesh is designed to resolve the thickness of the local EDL, and it is gradually stretched with a maximum stretching factor of about 3% and smoothly tapered to a fixed mesh size away from the membrane. To confirm grid convergence, we employed two mesh resolutions given in Table 1.

We employ a second order time advancement scheme to solve for the evolution of concentration and momentum fields in time. Given the unsteady nature of the system and participation of small spatio-temporal scales, a small time step should be used to allow accurate capture of a full range of dynamical behavior of the system. Even with a robust solver, time steps larger than that dictated by the unsteady physics should not be used. Based on our investigation, the only region in the system that responds quasi-statically is the very thin inner EDL in which normal diffusion and electromigration balance each other quickly in response to a change in the adjacent environment. This corresponds to a negatively large eigenvalue in the linearized system, which asymptotically enforces the quasi-steady equations in this region. Therefore, one should consider a numerical scheme allowing for an intermediate time step size which could bypass transience of this fast quasi-steady region. This realization justifies the use of an implicit method for fluxes active in the inner region of EDL. Thus we use an implicit method for calculation of the wall normal diffusion and electromigration terms. The time discretized version of Eq. (1c) is:

Table 1
Computational grid sizes employed in Comsol-based and reference DNS codes for transient calculations of fully the coupled PNP and NS equations. The grids are matched via the number of DOF due to the fourth order interpolation functions used in the commercial software. The time step for both simulations is $\Delta t = 10^{-6}$ scaled by diffusion time L^2/D.

Mesh	Comsol		Reference DNS		DOF
	N_x	N_y	N_x	N_y	
1	170	95	320	180	345,600
2	320	180	600	340	1,224,000

$$\frac{3c^{n+1}-4c^{n}+c^{n-1}}{2\Delta t}=D\frac{\partial^2 c^{n+1}}{\partial y^2}+\frac{D}{V_T}\frac{\partial}{\partial y}\left[c^{n+1}\frac{\partial \phi^{n+1}}{\partial y}\right]+Other^{n} \quad (2)$$

where the superscripts with indices n and $n-1$ denote the time step levels corresponding to known current and previous states, respectively. The superscript index $n+1$ corresponds to the unknown next state. For simplicity we drop the charge superscripts $^{\pm}$ and describe our numerical methodology with the cation concentration denoted as c. The left hand side term represents a second order discretization of the time term at time t^{n+1}. The first two terms on the right-hand-side respectively represent diffusion and electromigration fluxes in the wall-normal direction. The last term on the right-hand-side represents the rest of the terms in Eq. (1c).

At this form, Eq. (2) is formally first order in time, since a portion of right-hand-side of Eq. (1c) is evaluated at time t^n instead of t^{n+1}. To solve this issue, we devised an iterative procedure by introducing a series of intermediate solutions c^*, which will merge to expected c^{n+1}. In the first iteration, c^* is guessed based on the previous time step solution, and by proper implicit implementation of stiff terms we ensure the convergence of our iteration loop. Proper rearrangement of terms leads to:

$$\begin{aligned}&\frac{3}{2\Delta t}\left[c^{*+1}-c^{*}\right]-D\frac{\partial^2}{\partial y^2}(c^{*+1}-c^{*})-\frac{D}{V_T}\\&\times\frac{\partial}{\partial y}\left[c^{*+1}\frac{\partial \phi^{*+1}}{\partial y}-c^{*}\frac{\partial \phi^{*}}{\partial y}\right]\\&=\frac{-c^{*}+4c^{n}-c^{n-1}}{2\Delta t}+RHS^{*}\end{aligned} \quad (3)$$

where RHS^* represents the full right-hand-side of Eq. (1c), evaluated based on latest updates of fields. The left hand side of this equation involves the unknown values denoted by superscript $^{*+1}$, which should be solved coupled with the following form of Eq. (1d):

$$-\varepsilon\nabla^2\phi^{*+1}-\rho_e^{*+1}=0 \quad (4)$$

in which $\rho_e=ze(c^+-c^-)$. If one chooses to use only one iteration, Eq. (3) will recover the same form as in Eq. (2). However, in the limit of converged iterations (i.e. $c^{*+1}=c^*$ and $\phi^{*+1}=\phi^*$), the left hand side of Eq. (3) drops, and one recovers the second order fully implicit solution to the system. The current form in Eq. (3) will ensure convergence under intermediate Δt's that would resolve the chaos but bypass the stiff quasi-steady inner EDL region. However, in its current form the left-hand-side of Eqs. (3) and (4) involve nonlinear terms and coupling in the tangential direction, and thus are very expensive to invert. The job of numerical analysis here is to design an approximate left-hand-side operator that converges quickly and is easy to compute its inverse.

The first approximation to the left-hand-side of Eq. (3) is to introduce a linearization of the nonlinear terms. We define $\delta c=c^{*+1}-c^{*}$ and $\delta\phi=\phi^{*+1}-\phi^{*}$.

$$\begin{aligned}&\left(\frac{3}{2\Delta t}-D\frac{\partial^2}{\partial y^2}\right)\delta c^{+}-\frac{D}{V_T}\frac{\partial}{\partial y}\left[\delta c^{+}\frac{\partial \phi^{*}}{\partial y}\right]-\frac{D}{V_T}\frac{\partial}{\partial y}\left[c^{+*}\frac{\partial \delta\phi}{\partial y}\right]\\&=\frac{-c^{*}+4c^{n}-c^{n-1}}{2\Delta t}+RHS^{*}\end{aligned} \quad (5)$$

where now we resume to indicate the charge of species, by superscript $^+$ since the notation is simplified. Eq. (5) together with modified version of Eq. (4) in δ-notation would present a linear system that couple $\delta c^{\pm}$ with $\delta\phi$, which may be solved in each iteration using a linear solver. However, the directional coupling due to presence of Laplacian operator in Eq. (4) still keeps the computation cost high. The last modification that allows the use of direct and fast solver is based on manipulation of the last term on the left-hand-side of Eq. (5). First, we add to the left-hand-side the non-stiff term $\frac{D}{V_T}\frac{\partial}{\partial x}(c^{+*}\frac{\partial\delta\phi}{\partial x})$. This is equivalent of treating part of electromigration flux in the tangential direction implicitly, and since the physics associated with this term is non-stiff, it does not affect the convergence of the solver. With this addition, the last term on the left-hand-side of Eq. (5) can be written as $\frac{D}{V_T}\nabla\cdot(c^{+*}\nabla\delta\phi)$. Applying the rule of derivative of product we arrive at:

$$\frac{D}{V_T}\nabla\cdot(c^{+*}\nabla\delta\phi)=\frac{D}{V_T}c^{+*}\nabla^2\delta\phi+\frac{D}{V_T}\nabla c^{+*}\cdot\nabla\delta\phi \quad (6)$$

Using the Poisson relation, laplacian of ϕ can now be represented in terms of total charge. Therefore the first term in Eq. (6) can be rewritten as $-\frac{Dc^{+*}}{\varepsilon V_T}\delta\rho_e$. A linearized perturbation analysis, with a uniform base state, reveals that this term is the sole term responsible for charge relaxation, with time scale $\tau=\frac{\varepsilon V_T}{2Dzec}=\frac{\lambda_D^2}{D}$. Our analysis indicate that keeping only this term and ignoring the second term in Eq. (6), provides a robust approximation to the left-hand-side operator without sacrificing its convergence. The final time-discrete system that is solved in the reference DNS code is:

$$\begin{aligned}&\left(\frac{3}{2\Delta t}-D\frac{\partial^2}{\partial y^2}\right)\delta c^{+}-\frac{D}{V_T}\frac{\partial}{\partial y}\left[\delta c^{+}\frac{\partial \phi^{*}}{\partial y}\right]-\frac{zeDc^{+*}}{V_T\varepsilon}(\delta c^{+}-\delta c^{-})\\&=\frac{-c^{*}+4c^{n}-c^{n-1}}{2\Delta t}+RHS^{*}\end{aligned} \quad (7)$$

In this equation the left hand side operator involves only local coupling between δc^+ and δc^- and directional coupling only in the wall normal direction. This system can be solved directly with a fast $O(N)$ method that utilizes a pentadiagonal matrix inversion routine. Before each iteration, the right hand, side of Eq. (7) requires updated potential and velocity fields. The potential field is computed from latest c^* by solving the full Poisson equation. The Laplacian operator can be inverted using the fast Fourier transform in the tangential direction and a tridiagonal solver in the wall normal direction. The momentum equation is discretized in time with an approach similar to the approach described for concentration. However, in this case the linearity of the operators involved and homogeneity of the mesh in the tangential direction, allow the use of Fourier transforms and eliminating the coupling in the tangential direction. In this case the full viscous term can be evolved implicitly. In each iteration after the aforementioned update of ϕ^*, the electrostatic force in the right-hand-side of Eq. (1a) is updated, and the momentum equation is solved to update $\boldsymbol{u}^*$. Then Eq. (7) is solved to update the concentration fields, and then the iteration is repeated by solving the Poisson system for ϕ^* corresponding to the new ion concentration field. By choosing only one iteration per time step, this method will reduce to a first order accurate scheme. With two iterations or higher, the method will be second order accurate. We typically run our simulations with three iterations per time-step, and have confirmed that such a strategy results in second order accuracy in both time and space via an extensive verification against a general form of the method of manufactured solution [61]. With this custom-built numerical method, fast algorithms such as fast Fourier transforms, and fast low-band Matrix solvers are utilized to minimize the computational cost per time step. Similar approaches have been in use for decades for simulation of other complex flows such as turbulent channel flows and boundary layers [62]. The disadvantage of our custom-built DNS code is the limitation to simple geometries and structured meshes, however, as we shall see, it provides significant speedup advantage that can be utilized for investigation of basic physics in simplified settings.

4. Results and discussion

The accuracy of both commercial and reference DNS codes have been verified using the method of manufactured solutions (MMS)

against a class of exact solutions [61]. These exact solutions are smooth functions constructed to our set of governing equations modified with forcing source terms. The maximum error (L_∞-error) and area-averaged error (L_2-error) for the velocity field $\boldsymbol{u}(x,y,t)$ and anion concentration $c^-(x,y,t)$ are computed in our error analysis. By refining the mesh, the error drops with a second order rate for the reference DNS code. Third-order convergence is obtained for Comsol. As a representative of our detailed convergence results, we present the L_2-error estimates for c^- in Table 2.

Table 2
L_2-error estimates of dimensionless anion concentration $c^-(x,y,t)/c_{bulk}$ calculated by the 2D manufactured solution versus spatial grid refinement. Here the number of DOF is matched for both codes at each grid resolution with the considerations of fourth order interpolation functions employed in Comsol code.

Comsol		Reference DNS	
$N_x \times N_y$	$L_2-error$	$N_x \times N_y$	$L_2-error$
483	3.7×10^{-4}	1800	2.6×10^{-3}
2021	4.4×10^{-5}	7200	6.4×10^{-4}
8075	6.8×10^{-6}	28,800	1.6×10^{-4}

In Fig. 2 we present instantaneous snapshots of the dimensionless anion concentration c^-/c_{bulk} with superimposed flow streamlines obtained from the reference DNS (Fig. 2 and the Comsol simulation (Fig. 2b) performed at $\Delta\phi = 3V$. In these simulations we match the number of degrees of freedom by employing a mesh with $N_x = 320$ and $N_y = 180$ in the reference DNS and $N_x = 170$ and $N_y = 95$ in the Comsol simulation (Table 1). To minimize the potential effects of numerical dissipation on Comsol results, we employ a maximum value of parameter $\alpha = 0.99$ in the Generalized-α solver settings. We qualitatively compare the time evolution of electrohydrodynamic instability predicted by both codes. In the Supplemental material, we present movies from both simulations as well as the instantaneous snapshots of the evolution of free charge density.

At very early times (<0.0015) the anion concentration field has a diffusive nature revealing a depletion layer with a net free charge, as in Fig. 1c. However the instability starts to develop in time leading to distortions in the quiescent structure of anion concentration field (Fig. 2a and b at $t = 0.0015$). As the flow streamlines indicate, high concentration fluid (≈1) is advected towards the ion selective surface and low concentration fluid (≈0) is advected towards the

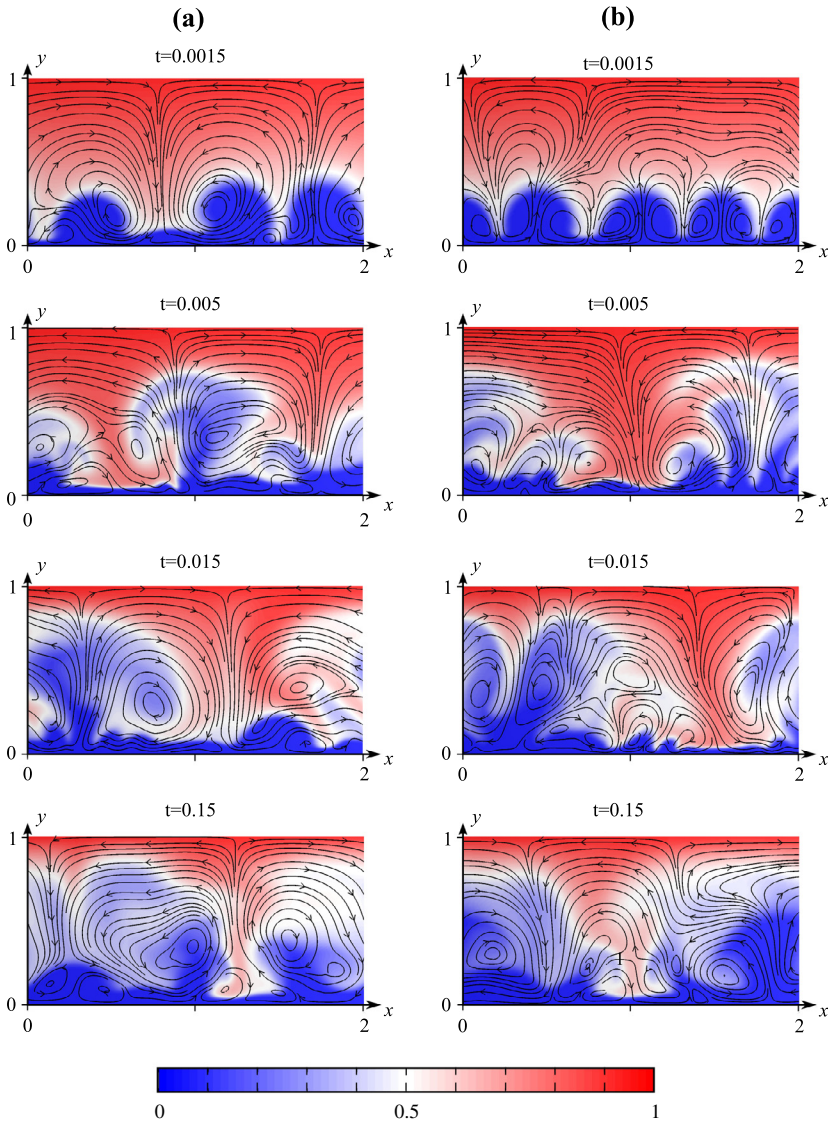

Fig. 2. Comparison of instantaneous contour plots of dimensionless anion concentration field c^-/c_{bulk} superimposed with flow lines (a) obtained from reference DNS code and (b) obtained by commercial Comsol Multiphysics code. Here $\Delta\phi = 120V_T$ and time is scaled by diffusion time L^2/D. To enhance the visualization of small structures, we plot $(c^-/c_{bulk})^{1/3}$. The DOF solved for in both codes are matched by proper selection of grid resolution.

bulk of the solution. At intermediate times (second and third panels in Fig. 2), the strength of the vortices grow in time. Thereby the outflow of the low concentration fluid extends further towards the bulk. Besides, patches of negative charge emerge from the initially positive free charge ρ_e layer adjacent to the ion selective boundary. At a long enough time (here shown at $t = 0.15$), instability is fully developed. Both simulations predict strong spatio-temporal variations in concentration and flow fields indicative of the chaotic nature of the electrokinetic phenomena studied at $\Delta\phi = 3V$. Our observations reveal that the instantaneous fields obtained from both codes are in qualitative agreement as well as consistent with previous findings [9,63]. Due to the chaotic nature of flows arising from electrokinetic instabilities, the instantaneous flow patterns and the anion concentration distributions are not one-to-one matching given the randomness of the initial perturbations.

Electric response of electrochemical systems are indicative of global ion transport properties and frequently measured by chronopotentiometry or chronoamperometry techniques at constant applied current or constant applied voltage, respectively. Here we calculate the current density $\boldsymbol{i}(x,y,t) = \boldsymbol{j}_{c^+} - \boldsymbol{j}_{c^-}$ where $\boldsymbol{j}_{c^+}$ and $\boldsymbol{j}_{c^-}$ are ion fluxes of cations and anions, respectively, driven by advection, diffusion and electromigration. Thereby these are described as $\boldsymbol{j}_{c^\pm} = c^\pm \boldsymbol{u} - D\nabla c^\pm \mp DV_T^{-1} c^\pm \nabla\phi$. Moreover we calculate the surface-averaged current density $\langle \boldsymbol{i} \rangle_\Omega(t)$ as well as both time and space averaged current density $\boldsymbol{I}$.

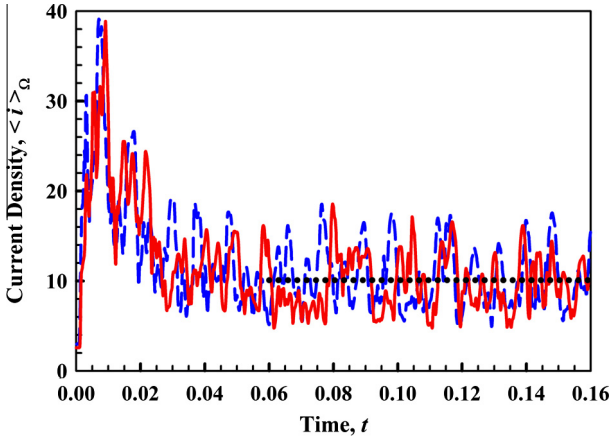

Fig. 3. Surface-averaged current density through the ion-selective interface for $\Delta\phi = 3V$. Reference DNS (blue dash line, — —) and Comsol simulation (red solid line, ——). Horizontal black dotted line depicts the time and space averaged current density evaluated from $t = 0.06$ to $t = 0.16$. Time is scaled by diffusion time L^2/D. The current density is nondimensional and calculated from the $c^\pm$ scaled by c_{bulk}, $\boldsymbol{u}$ scaled by diffusion velocity D/L and ϕ scaled by thermal voltage V_T. (For interpretation of the references to color in this figure legend, the reader is referred to the web version of this article.)

Fig. 3 shows that the current density $\langle \boldsymbol{i} \rangle_\Omega$ behaves highly oscillatory in time. Both simulations predict a transient current until $t \approx 0.05$ and then a statistically stationary, yet chaotic, state is reached. Fully chaotic multi-layer vortex structures as shown in Fig. 2 induce rapid fluctuations in the current density. The dynamic current density profiles shown in Fig. 3 are in good statistical agreement. The black dotted line in Fig. 3 depicts the time and space averaged current density calculated for $0.06 < t < 0.16$ in the statistically stationary state. Both codes predicted the same average current density equal to 10.1 $Dc_{bulk}ze/L$.

The applied potential value of $\Delta\phi = 3V$ has been specifically chosen in this study because the high electric forcing induces highly chaotic geometric features over a wide range of length scales. Therefore, computation of this regime is most challenging, and thus it is suitable for assessment of performance of commercial software. To best present the wide range of length scales and the most distinct chaotic features in the current model problem, we compute the one-dimensional spatial power spectral density of anion concentration c^- and velocity $\boldsymbol{u}$ in the homogenous direction. The details of the spectral density calculations are provided in Appendix A.

We plot spatial spectra of anion concentration c^- (Fig. 3 and kinetic energy (Fig. 4b) in the x- direction at fixed wall normal distances $y = 0.025$, 0.1 and 0.4. The spectral density of anion concentration shows the distribution of anions in a broad range of wavenumbers. Likewise, energy spectral density shows the distribution of the kinetic energy in the flow over a range of different scales. Comsol simulations predict broadband structure of both quantities in agreement with the reference DNS and previous reports [9,63]. It is important to note here that there is no inertial range in the spectra of velocity due to low Reynolds number. The chaotic flow is sustained without the need of inertia unlike in traditional turbulent flows.

We compare these detailed statistics obtained from the reference DNS and Comsol simulations and show the effect of mesh resolution for both codes. With the considerations of fourth order interpolation functions employed in the Comsol code, we keep the spatial resolution fairly equivalent by means of matching the

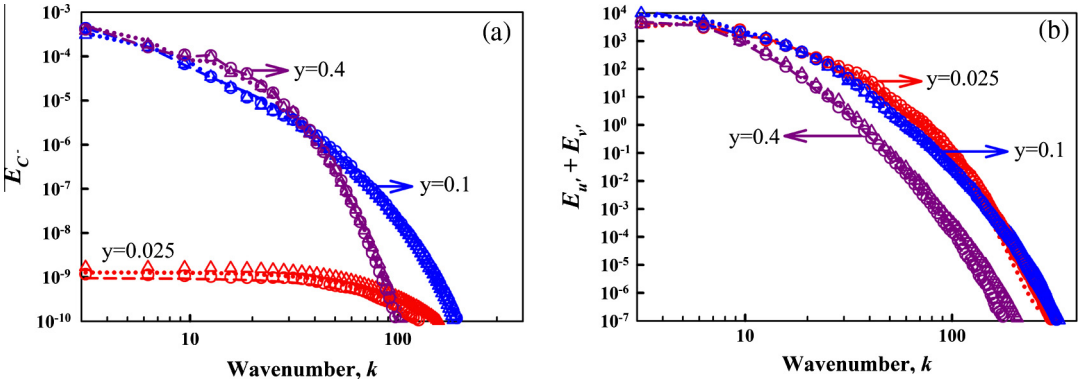

Fig. 4. Broadband spatial spectra of (a) anion concentration c^- and (b) kinetic energy at different wall-normal positions and at different mesh resolutions with matched number of DOF in the reference DNS and the Comsol simulation. Symbols represent the reference DNS results for coarser mesh with $N_x = 320$ and $N_y = 180$ (open triangles △) and for finer mesh with $N_x = 600$ and $N_y = 340$ (open circles ○). Lines represent Comsol results for coarser mesh with $N_x = 170$ and $N_y = 95$ (dotted lines ···) and for finer mesh with $N_x = 320$ and $N_y = 180$ (dashed lines — —). Here Generalized-α time stepping is used with $\alpha = 0.8$ in Comsol simulations. Colors show the wall-normal distance which are also indicated by arrows both in (a) and (b). Red: $y = 0.025$, blue: $y = 0.1$, purple: $y = 0.4$. (For interpretation of the references to color in this figure legend, the reader is referred to the web version of this article.)

number of DOF instead of the grid points in our mesh convergence analysis. We employ two grid resolutions, a coarser mesh and a finer mesh described as Mesh 1 and Mesh 2 in Table 1, respectively. Accordingly Mesh 1 (Table 1) has a minimum $\Delta y = 3.5 \times 10^{-4}$ and a maximum $\Delta y = 1.7 \times 10^{-2}$. Mesh 2 has a minimum $\Delta y = 9.6 \times 10^{-5}$ and a maximum $\Delta y = 4.7 \times 10^{-3}$. Here all grid sizes are scaled by L.

The hydrodynamic instabilities are dominantly triggered at close proximity to the ion selective boundary since considerable free charge exists there. The anion concentration in this region can have very small values due to CP depletion, but it often sustains small scale features in both lateral and transverse directions. (Fig. 2) Grid convergence near $y = 0$ is critical to resolve the EDL and the highly irregular charged region next to it. The spatial spectra of concentration (Fig. 4a) and velocity (Fig. 4b) calculated at $y = 0.025$ show a well-resolved mesh though slight variations are observed in the concentration spectra. At intermediate wall-normal distance $y = 0.4$, spatial spectra of both concentration and energy are well converged at both mesh resolutions. Furthermore, the spectral densities calculated from both codes overlap in the full range of wavenumbers, clearly showing good quantitative agreement between the two codes at the presented settings.

As mentioned earlier, in computational algorithms, the requirements of accuracy, efficiency, and robustness are often not all aligned. Considering the fact that robustness is often ensured by the addition of numerical dissipation in general purpose CFD software, we next present the impact of numerical dissipation on the prediction of chaotic electrokinetic transport. We control the numerical damping by means of varying the α parameter ($0 \leqslant \alpha \leqslant 1$) in the generalized-$\alpha$ time stepping method, where several values of α are employed ($= 0.1, 0.4, 0.8, 0.99$) inducing more damping for smaller values of α.

Fig. 5 shows one-dimensional anion concentration spectra at selected y-positions obtained at different numerical damping implemented via the employed temporal discretization scheme. At intermediate y (=0.1 and =0.4), the same anion concentration distribution has been predicted for all the wavenumber range irrespective of α. This is mainly because these regions are dominated by large and slow scales, and thus are well resolved. The vicinity of the membrane, however, is dominated by high-frequency oscillations and the results are highly sensitive to numerical damping. As shown in Fig. 5, the spectral content can be mispredicted by almost an order of magnitude over a wide range of wavenumbers. This discrepancy results in severe underprediction of mean square fluctuating quantities due to numerical dissipation. For example at $y = 0.025, \alpha = 0.1$ leads to underprediction of mean square anion concentration by as much as $\sim 79\%$ compared to that obtained when $\alpha = 0.99$. These variations in the detailed statistics reflect on the predicted global current density $\boldsymbol{I}$. Numerical damping of $\alpha = 0.1$ results in $\sim 5\%$ less current density $\boldsymbol{I}$ compared to that obtained by the simulation with minimal damping of $\alpha = 0.99$ and by the reference DNS.

These levels of sensitivity to numerical damping are comparable to (even more severe than) the sensitivities previously reported in simulations of standard turbulence. For example, in the results of Mittal and Moin [42] who investigated simulations of turbulent flows past a circular cylinder and reported impact of numerical dissipation on the spectra, mean square quantities, as well as the global statistics. Similar to our results, they reported that the high-frequency content of the spectrum can be under-predicted by order(s) of magnitude. Their findings indicated $\approx$ 20–30% deviation in the prediction of mean square velocity, when a dissipative method was used for the simulation of turbulence. In terms of global statistics, they reported 2% of deviation in the predicted drag coefficients, which is less sensitive compared to what we observe here for mean current density ($\sim 5\%$).

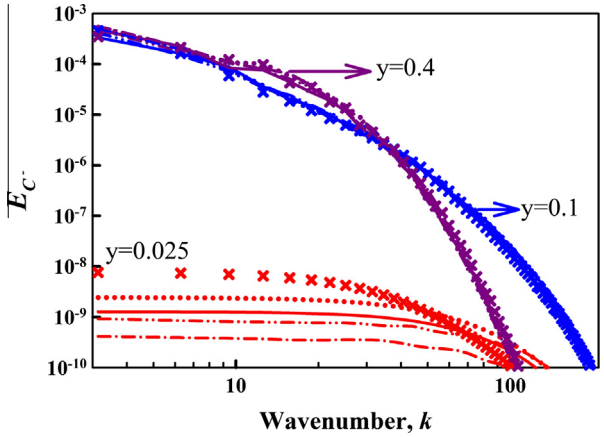

Fig. 5. Effect of numerical dissipation and time discretization method on one-dimensional anion concentration spectra. Symbols represent time-discrete method and lines represent generalized-α method with different numerical damping. $\alpha = 0.99$ dotted lines ($\cdots$), $\alpha = 0.8$ solid lines (—), $\alpha = 0.4$ dash-dot-dot lines (—$\cdot\cdot$), $\alpha = 0.1$ dash-dot lines (—$\cdot$). Colors show the wall-normal distance which are also indicated by arrows, red: $y = 0.025$, blue: $y = 0.1$, purple: $y = 0.4$. (For interpretation of the references to color in this figure legend, the reader is referred to the web version of this article.)

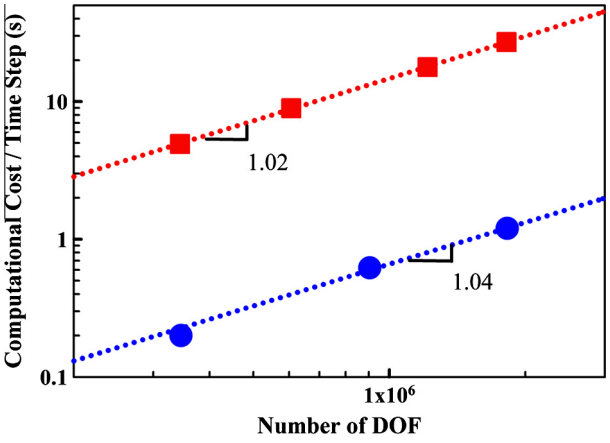

Fig. 6. CPU time per time step required by Comsol-based code (squares ■) and by reference DNS code (circles ●) with respect to number of degrees of freedom solved for. Dotted lines reveal linear regression with the slopes depicted. Compared CPU times are obtained using a single core, excluding parallelization efficiencies.

Among other readily built-in time-stepping methods provided by Comsol Multiphysics, we present results obtained by a time-discrete method, utilizing second order backward differentiation, in comparison to those by generalized-α method (Fig. 5). Our results are indicative of the sensitivity of detailed statistics to the employed time-stepping algorithm.

To further assess the performance of the employed commercial solver, we compare the CPU-time required to solve per time step by the Comsol simulation and the reference DNS. A linear increase in computational cost is obtained for both codes with respect to increase in the number of degrees of freedom (Fig. 6). However the Comsol code is at least 20 times slower than the custom-built reference code developed specifically for predicting electrokinetic chaos. This is expected, since general purpose codes often treat the entire physics implicitly, and thus invert a global matrix associated with the coupling of all physics in all directions. Such matrices have a high bandwidth and thus their inversion takes much longer than the inversion of tridiagonal and pentadiagonal matrices employed in the custom-built reference DNS code. The factor

of 20 speedup obtained by the custom-built DNS code is crucial for large-scale three-dimensional simulations. It is important to note that presented runtimes are obtained using a single core. In a preliminary investigation, we compared the parallelization efficiencies. Comparison of the runtimes of both codes running on 8 cores indicated that the custom-built DNS code was about ~ 160 times faster than Comsol. This is due to the ability of the custom-built DNS code to scale linearly on parallel hardware, while Comsol was not able to scale efficiently for this problem.

5. Conclusions

We have investigated whether a general-purpose commercial CFD software can accurately and efficiently predict transient chaotic electrokinetic phenomena. As a benchmark analysis, we compared the results with those obtained by non-dissipative central-difference schemes employed in a custom-built DNS code tailored for unsteady electrokinetic flows. We presented a novel numerical treatment used in the custom-built DNS code that allowed efficient calculations of unsteady electrokinetic transport. We also discussed the physical reasoning behind this numerical treatment.

High-order statistics revealed sensitivity to numerical damping in the vicinity of ion-selective boundary. As a consequence, fluctuating quantities are significantly under-predicted by almost an order of magnitude. Global statistics are also affected by numerical damping, *e.g.* current density is under-predicted by about 5%. These findings reveal that the impact of numerical dissipation in electrokinetic chaos is comparable, but slightly more severe, than that in traditional turbulent flows. When numerical dissipation is minimized, the results predicted by the commercial solver are in good quantitative agreement with those obtained by custom DNS however the commercial solver requires at least a 20 times higher computational expense.

We should note that the computational domain in this study has been chosen to be small enough that a single core is sufficient for the simulations with a reasonable solution time. We have resolved a small domain in close proximity of a cation selective surface. Whereas realistic systems require resolving much larger domains and often include several stacks of anion selective and cation selective surfaces such as the processes in desalination and electrodialysis based industries. Our comparative results are in 2D while the effects of three dimensionality and confinement are crucial in industrial systems. Parallel computing is essential for reducing the computational cost of simulations of industrial applications.

Acknowledgments

Grant from NWO (Rubicon, Post-Doctoral fellowship for E.K.) is gratefully acknowledged. The authors would like to thank Mathias B. Andersen for helpful discussions on the implementation of both commercial and reference DNS codes.

Appendix A. Calculation of spectral densities

We introduce the decomposition of the corresponding quantity into its average and fluctuating components. For instance the anion concentration is given as $c^-(x,y,t) = \overline{c^-}(y,t) + c^{-\prime}(x,y,t)$ where $\overline{c^-}(y,t)$ is x-averaged anion concentration and $c^{-\prime}(x,y,t)$ is the anion concentration fluctuation. We calculate the Fourier transform $\hat{c^-}(k_x,y,t)$ of the fluctuating component $c^{-\prime}(x,y,t)$. For a fixed wall normal distance y,

$$\hat{c^-}(k_x,t) = \frac{1}{2\pi L}\int_0^L c^{-\prime}(x,t)e^{ik_x}dx \tag{A.1}$$

where k_x is the x component of the wavenumber. ($\Delta k_x = 2\pi/L_x$) The spectral density of the anion concentration E_{c^-} at a fixed y – is the square of the absolute value of its Fourier transform;

$$E_{c^-}(k_x) = \frac{\Delta x^2}{2\pi L}|\hat{c^-}(k_x,t)|^2 \tag{A.2}$$

Similarly we calculate the energy spectral density of each velocity component u and v. ($E_{u'u'}(k_x)$ for u and $E_{v'v'}(k_x)$ for v) To achieve additional statistical convergence, we average the spectral density of a corresponding quantity in time in a sufficiently large time interval in a statistically stationary state.

Appendix B. Supplementary material

Supplementary data associated with this article can be found, in the online version, at http://dx.doi.org/10.1016/j.jcis.2014.12.081.

References

[1] N. Mishchuk, Adv. Colloid Interface Sci. 160 (1–2) (2010) 16–39, http://dx.doi.org/10.1016/j.cis.2010.07.001.
[2] V.V. Nikonenko, A.V. Kovalenko, M.K. Urtenov, N.D. Pismenskaya, J. Han, P. Sistat, G. Pourcelly, Desalination 342 (2014) 85–106, http://dx.doi.org/10.1016/j.desal.2014.01.008.
[3] F.C. Leinweber, M. Pfafferodt, A. Seidel-Morgenstern, U. Tallarek, Anal. Chem. 77 (18) (2005) 5839–5850, http://dx.doi.org/10.1021/ac050609o.
[4] P.M. Biesheuvel, M.Z. Bazant, Phys. Rev. E 81 (3) (2010) 031502, http://dx.doi.org/10.1103/PhysRevE.81.031502.
[5] A. Höltzel, U. Tallarek, J. Sep. Sci. 30 (10) (2007) 1398–1419, http://dx.doi.org/10.1002/jssc.200600427.
[6] J.D. Posner, C.L. Pérez, J.G. Santiago, Proc. Nat. Acad. Sci. 109 (36) (2012) 14353–14356, http://dx.doi.org/10.1073/pnas.1204920109. arXiv: http://www.pnas.org/content/109/36/14353.full.pdf+html.
[7] G. Garcia-Schwarz, M. Bercovici, L.A. Marshall, J.G. Santiago, J. Fluid Mech. 679 (2011) 455–475.
[8] G.R. Wang, F. Yang, W. Zhao, Lab Chip 14 (8) (2014) 1452–1458, http://dx.doi.org/10.1039/c3lc51403j.
[9] C.L. Druzgalski, M.B. Andersen, A. Mani, Phys. Fluids 25 (2013) 110804.
[10] S. Abdu, M.-C. Martí-Calatayud, J.E. Wong, M. García-Gabaldón, M. Wessling, ACS Appl. Mater. Interfaces 6 (3) (2014) 1843–1854, http://dx.doi.org/10.1021/am4048317. arXiv:http://pubs.acs.org/doi/pdf/10.1021/am4048317.
[11] M.B. Andersen, D.M. Rogers, J. Mai, B. Schudel, A.V. Hatch, S.B. Rempe, A. Mani, Langmuir: ACS J. Surf. Colloids 30 (26) (2014) 7902–7912, http://dx.doi.org/10.1021/la5014297.
[12] G. Marshall, E. Mocskos, G. González, S. Dengra, F. Molina, C. Iemmi, Electrochim. Acta 51 (15) (2006) 3058–3065, http://dx.doi.org/10.1016/j.electacta.2005.08.040.
[13] Y.-M. Lee, S.-J. Lee, C.-Y. Lee, D.-Y. Chang, J. Power Sources 193 (1) (2009) 227–232, http://dx.doi.org/10.1016/j.jpowsour.2009.03.042.
[14] T.A. Zangle, A. Mani, J.G. Santiago, Chem. Soc. Rev. 39 (3) (2010) 1014–1035, http://dx.doi.org/10.1039/b902074h.
[15] Y. Green, S. Shloush, G. Yossifon, Phys. Rev. E Stat. Nonlinear Soft Matter Phys. 89 (4) (2014) 043015.
[16] S.J. Kim, Y.-A. Song, J. Han, Chem. Soc. Rev. 39 (3) (2010) 912–922, http://dx.doi.org/10.1039/b822556g.
[17] M. Mulder, Basic Principles of Membrane Technology, Springer Netherlands, Dordrecht, 1996, http://dx.doi.org/10.1007/978-94-009-1766-8.
[18] K. Kontturi, L. Murtomäki, J. Manzanares, Ionic Transport Processes: in Electrochemistry and Membrane Science: in Electrochemistry and Membrane Science, OUP Oxford, 2008.
[19] T. Matsuura, T. Fane, R. Kwak, G. Guan, W.K. Peng, J. Han, Desalination 308 (2013) 138–146.
[20] S. Rubinstein, G. Manukyan, A. Staicu, I. Rubinstein, B. Zaltzman, R. Lammertink, F. Mugele, M. Wessling, Phys. Rev. Lett. 101 (23) (2008) 236101, http://dx.doi.org/10.1103/PhysRevLett.101.236101.
[21] F. Maletzki, H.-W. Rösler, E. Staude, J. Membr. Sci. 71 (1) (1992) 105–116.
[22] J. Krol, J. Membr. Sci. 162 (1–2) (1999) 145–154, http://dx.doi.org/10.1016/S0376-7388(99)00133-7.
[23] R. Kwak, V.S. Pham, K.M. Lim, J. Han, Phys. Rev. Lett. 110 (11) (2013) 114501, http://dx.doi.org/10.1103/PhysRevLett.110.114501.
[24] H.-C. Chang, G. Yossifon, E.a. Demekhin, Annu. Rev. Fluid Mech. 44 (1) (2012) 401–426, http://dx.doi.org/10.1146/annurev-fluid-120710-101046.
[25] V. Fleury, J.-N. Chazalviel, M. Rosso, Phys. Rev. Lett. 68 (16) (1992) 2492–2495, http://dx.doi.org/10.1103/PhysRevLett.68.2492.
[26] I. Rubinstein, B. Zaltzman, Math. Models Methods Appl. Sci. 11 (02) (2001) 263–300, http://dx.doi.org/10.1142/S0218202501000866.
[27] B. Zaltzman, I. Rubinstein, J. Fluid Mech. 579 (2007) 173, http://dx.doi.org/10.1017/S0022112007004880.
[28] K.T. Chu, M.Z. Bazant, SIAM J. Appl. Math. 65 (5) (2005) 1485–1505, http://dx.doi.org/10.1137/040609926.

[29] E. Yariv, Phys. Rev. E 80 (5) (2009) 051201, http://dx.doi.org/10.1103/PhysRevE.80.051201.
[30] M. Bazant, T. Squires, Phys. Rev. Lett. 92 (6) (2004) 066101, http://dx.doi.org/10.1103/PhysRevLett.92.066101.
[31] J.A. Manzanares, S. Mafd, H.J. Reiss, J. Phy. Chem. 97 (1993) 8524–8530.
[32] I. Rubinstein, B. Zaltzman, Phys. Rev. E 62 (2) (2000) 2238–2251, http://dx.doi.org/10.1103/PhysRevE.62.2238.
[33] E.A. Demekhin, V.S. Shelistov, S.V. Polyanskikh, Phys. Rev. E 84 (3) (2011) 036318.
[34] E.A. Demekhin, N.V. Nikitin, V.S. Shelistov, Phys. Fluids 25 (12) (2013) 122001, http://dx.doi.org/10.1063/1.4843095.
[35] V.S. Pham, Z. Li, K.M. Lim, J.K. White, J. Han, Phys. Rev. E 86 (4) (2012) 046310, http://dx.doi.org/10.1103/PhysRevE.86.046310.
[36] C.L. Druzgalski, A. Mani, Bull. Am. Phys. Soc. 67 (2014).
[37] E.A. Demekhin, N.V. Nikitin, Phys. Rev. E 90 (2014) 013031.
[38] G. Iaccarino, J. Fluids Eng. 123 (4) (2001) 819–828.
[39] C.J. Freitas, J. Fluids Eng. 117 (2) (1995) 208–218.
[40] P. Tucker, IEEE Trans. Part A 20 (4) (1997) 518–529.
[41] T. Glatzel, C. Litterst, C. Cupelli, T. Lindemann, C. Moosmann, R. Niekrawietz, W. Streule, R. Zengerle, P. Koltay, Comput. Fluids 37 (3) (2008) 218–235, http://dx.doi.org/10.1016/j.compfluid.2007.07.014.
[42] R. Mittal, P. Moin, AIAA J. 35 (8) (1997) 1415–1417, http://dx.doi.org/10.2514/2.253.
[43] M.P. Beaudan Patrick, Numerical experiments on the flow past a circular cylinder at sub-critical reynolds number, Tech. rep., Report No. TF-62, Department of Mechanical Engineering, Stanford University, 1994.
[44] A.G. Kravchenko, P. Moin, Phys. Fluids 12 (2) (2000) 403.
[45] P. Catalano, M. Wang, G. Iaccarino, P. Moin, Int. J. Heat Fluid Flow 24 (4) (2003) 463–469, http://dx.doi.org/10.1016/S0142-727X(03)00061-4.
[46] M. Breuer, Int. J. Heat Fluid Flow 19 (5) (1998) 512–521.
[47] S. Pope, Turbulent Flows, Cambridge University Press, 2000.
[48] P. Dechadilok, W.M. Deen, J. Membr. Sci. 336 (1–2) (2009) 7–16.
[49] R. Chein, H. Chen, C. Liao, J. Membr. Sci. 342 (1–2) (2009) 121–130.
[50] J. Hrdlička, N.S. Patel, D. Snita, Electrophoresis 35 (12–13) (2014) 1790–1794.
[51] D. Bottenus, Y.-J. Oh, S.M. Han, C.F. Ivory, Lab Chip 9 (2) (2009) 219–231.
[52] T. Postler, Z. Slouka, M. Svoboda, M. Pribyl, D. Snita, J. Colloid Interface Sci. 320 (1) (2008) 321–332.
[53] S. Qian, Y. Ai, Electrokinetic Particle Transport in Micro-/Nanofluidics: Direct Numerical Simulation Analysis, Surfactant Science, Taylor & Francis, 2012.
[54] E.J. Dickinson, H. Ekström, E. Fontes, Electrochem. Commun. 40 (0) (2014) 71–74, http://dx.doi.org/10.1016/j.elecom.2013.12.020.
[55] K.B. Deshpande, Electrochim. Acta 56 (4) (2011) 1737–1745.
[56] C.P. Nielsen, H. Bruus, Phys. Rev. E 89 (4) (2014) 042405.
[57] C.P. Nielsen, H. Bruus, Concentration polarization, surface currents, and bulk advection in a microchannel, arXiv:1408.4610 [physics.flu-dyn] (2014) 15arXiv:1408.4610.
[58] M.C.D. Soni Gaurav, T.M. Squires, Study of nonlinear effects in electrokinetics, in: Excerpt from the Proceedings of the COMSOL Conference 2007, Boston.
[59] M. Urtenov, A. Uzdenova, A. Kovalenko, V. Nikonenko, N. Pismenskaya, V. Vasil'eva, P. Sistat, G. Pourcelly, J. Membr. Sci. 447 (2013) 190–202.
[60] Comsol Multiphysics Reference Manual for Version 4.4, November 2013.
[61] S. Kambiz, K. Patrick, Code verification by the method of manufactured solutions, Technical Report SAND2000-1444, Sandia National Laboratories, 2000.
[62] J. Kim, P. Moin, R. Moser, J. Fluid Mech. 177 (1) (1987) 133–166.
[63] S.M. Davidson, M.B. Andersen, A. Mani, Phys. Rev. Lett. 112 (12) (2014) 128302, http://dx.doi.org/10.1103/PhysRevLett.112.128302.